Square skyrmion crystal in centrosymmetric itinerant magnets

Satoru Hayami and Yukitoshi Motome

Department of Applied Physics, the University of Tokyo, Tokyo 113-8656, Japan

We theoretically investigate the origin of the square-type skyrmion crystal in centrosymmetric itinerant magnets, motivated from the recent experimental finding in $GdRu_2Si_2$ [N. D. Khanh *et al.*, Nat. Nanotech. **15**, 444 (2020)]. By simulated annealing for an effective spin model derived from the Kondo lattice model on a square lattice, we find that a square skyrmion crystal composed of a superposition of two spin helices is stabilized in a magnetic field by synergy between the positive biquadratic, bond-dependent anisotropic, and easy-axis anisotropic interactions. This is in stark contrast to triangular skyrmion crystals which are stabilized by only one of the three, suggesting that the square skyrmion crystal is characteristic of itinerant magnets with magnetic anisotropy. We also show that a variety of noncollinear and noncoplanar spin textures appear depending on the model parameters as well as the applied magnetic field. The present systematic study will be useful not only for identifying the key ingredients in $GdRu_2Si_2$ but also for exploring further skyrmion-hosting materials in centrosymmetric itinerant magnets.

I. INTRODUCTION

A magnetic skyrmion has attracted great interest owing to rich physics emerging from its topological spin texture[1–7]. For example, a periodic arrangement of the skyrmions, which is referred to as the skyrmion crystal (SkX), gives rise to a giant topological Hall effect[8–10], Nernst effect[11,12], and nonreciprocal transport[13,14] through the spin Berry phase mechanism[15–17]. The topological robustness and unconventional transport properties may provide potential applications to next-generation magnetic memory and logic computing devices in spintronics[7,18,19]. While many materials have been found to host the skyrmions thus far, they have been mostly limited to the materials with noncentrosymmetric lattice structures and strong spin-orbit coupling. In fact, the SkXs were observed in chiral and polar magnets[20–29] where the spin-orbit coupling generates the Dzyaloshinskii-Moriya interaction[30,31].

Recently, several SkXs exhibiting the giant topological Hall and Nernst effects were discovered also in centrosymmetric f-electron compounds, such as triangular-type SkXs in Gd_2PdSi_3[32–34] and $Gd_3Ru_4Al_{12}$[35], and a square-type SkX in $GdRu_2Si_2$[36,37]. Due to the centrosymmetric lattice structures, their origin might be attributed to magnetic frustration[38–42] or effective magnetic interactions arising from the spin-charge coupling between conduction and localized electrons[43–47] rather than the DM interaction. In particular, $GdRu_2Si_2$ can be a prototype for the SkX originating from the spin-charge coupling, since the crystal structure is tetragonal that is free from geometrical frustration. Although the origin was speculated to be four-spin interactions mediated by itinerant electrons in the presence of easy-axis anisotropy[36], it has not been fully clarified yet from the microscopic point of view.

In the present study, we theoretically examine an instability toward the square SkX on a centrosymmetric tetragonal lattice in itinerant magnets. By performing simulated annealing for an effective spin model which incorporates the itinerant nature of electrons, we show that the square SkX is stabilized by the interplay among the four-spin biquadratic interaction, bond-dependent anisotropic interaction, and easy-axis anisotropic interaction in a magnetic field. The SkX is a double-Q state composed of a superposition of two spin helices, similar to the one observed in $GdRu_2Si_2$[36]. We find that the SkX exhibits a larger scalar spin chirality, which leads to a stronger topological Hall response, for a larger biquadratic interaction and smaller bond-dependent anisotropy. Besides the square SkX, we find several noncollinear and noncoplanar spin states depending on the model parameters. In particular, different types of double-Q states, which appear next to the square SkX upon increasing or decreasing the magnetic field, well explain the experimental results in $GdRu_2Si_2$[36,37]. We also discuss the stability of the square SkX in comparison with that of triangular SkXs; the interplay among the biquadratic, bond-dependent, and easy-axis anisotropic interactions plays an important role in the square SkX, whereas only one of them can stabilize the triangular ones. Our systematic analyses would be a reference to further exploration of skyrmion-hosting materials in centrosymmetric itinerant magnets.

The rest of the paper is organized as follows. In Sec. II, we introduce the effective spin model with the biquadratic and anisotropic interactions, and the numerical method to investigate the ground state. We discuss the magnetic phase diagram at zero field in Sec. III. In Sec. IV, we show the results in a magnetic field and identify the key ingredients for the square SkX. We discuss the results in comparison with the experiments for $GdRu_2Si_2$ in Sec. V. We also compare the stability of the square SkX with the triangular one. Section VI is devoted to the summary. In Appendix A, we show the effect of the magnetic field on the double-Q state which is not focused on in the main text.

II. MODEL AND METHOD

We consider an effective spin model on the basis of the Kondo lattice model consisting of itinerant electrons and localized spins[37,46,48–50], whose Hamiltonian is given by

$$\mathcal{H} = 2\sum_{\boldsymbol{q}} \left(-J\lambda_{\boldsymbol{q}} + \frac{K}{N}\lambda_{\boldsymbol{q}}^2 \right) - H\sum_i S_i^z, \quad (1)$$

with

$$\lambda_{\boldsymbol{q}} = \sum_{\alpha\beta} \Gamma_{\boldsymbol{q}}^{\alpha\beta} S_{\boldsymbol{q}}^{\alpha} S_{-\boldsymbol{q}}^{\beta}, \tag{2}$$

where the localized spins $\boldsymbol{S}_i$ at site i form a square lattice with the number of spins N. We regard $\boldsymbol{S}_i$ as a classical spin with a fixed length $|\boldsymbol{S}_i| = 1$ for simplicity. $\boldsymbol{S}_{\boldsymbol{q}}$ is the Fourier transform of $\boldsymbol{S}_i$. The first term in Eq. (1) consists of the bilinear and biquadratic interactions in momentum ($\boldsymbol{q}$) space, whose coupling constants are represented by J and K, respectively. $\Gamma_{\boldsymbol{q}}^{\alpha\beta}$ in Eq. (2) is a $\boldsymbol{q}$-dependent dimensionless form factor to represent the magnetic anisotropy that satisfies the fourfold rotational symmetry of the square lattice[37]. The second term in Eq. (1) represents the Zeeman coupling to an external magnetic field H along the z direction.

The effective spin model with the momentum-space interactions is obtained from the Kondo lattice model by using the perturbation expansion in terms of the spin-charge coupling between itinerant electrons and localized spins[44–46,51]. The bilinear term is derived from the lowest-order expansion, which is referred to as the Ruderman-Kittel-Kasuya-Yosida (RKKY) interaction[52–54]. Meanwhile, the biquadratic term is one of the second lowest-order contributions, which plays a crucial role in stabilizing noncoplanar spin textures composed of superpositions of multiple helices[46]. The other contributions are ignored by assuming distinct peak structures of the bare susceptibility[46]. The coupling constants J and K depend on the electronic state of the itinerant electrons, such as the band filling and hopping parameters. We regard them as independent parameters in the following calculations, and take $J = 1$ as an energy unit and $K > 0$.

In order to investigate the magnetic phase diagram in the model in Eq. (1), we simplify the interaction term by focusing on the situation where the magnetic bare susceptibility of the itinerant electrons shows maxima at $\boldsymbol{Q}_1 = (Q, 0)$ and $\boldsymbol{Q}_2 = (0, Q)$, which are compatible with the fourfold rotational symmetry. We take $Q = \pi/3$ without loss of generality. In other words, we ignore the contributions from the interactions except for $\boldsymbol{Q}_1$ and $\boldsymbol{Q}_2$. Then, only the form factors at $\boldsymbol{Q}_1$ and $\boldsymbol{Q}_2$, $\Gamma_{\boldsymbol{Q}_1}$ and $\Gamma_{\boldsymbol{Q}_2}$, are taken into account, which are given by

$$\Gamma_{\boldsymbol{Q}_1} = \begin{pmatrix} \Gamma^{\mathrm{iso}} - I^{\mathrm{BA}} & 0 & 0 \\ 0 & \Gamma^{\mathrm{iso}} + I^{\mathrm{BA}} & 0 \\ 0 & 0 & \Gamma^{\mathrm{iso}} + I^z \end{pmatrix},$$

$$\Gamma_{\boldsymbol{Q}_2} = \begin{pmatrix} \Gamma^{\mathrm{iso}} + I^{\mathrm{BA}} & 0 & 0 \\ 0 & \Gamma^{\mathrm{iso}} - I^{\mathrm{BA}} & 0 \\ 0 & 0 & \Gamma^{\mathrm{iso}} + I^z \end{pmatrix}. \tag{3}$$

Here, Γ^{iso} represents the isotropic form factor; we take $\Gamma^{\mathrm{iso}} = 1$. Meanwhile, I^{BA} and I^z represent the anisotropic form factors which are taken to be invariant under the fourfold rotational operation. These anisotropic interactions arise from the spin-orbit coupling under the crystalline electric field[48,55,56]. Their magnitudes and signs depend on the detailed electronic band structures. Hereafter, we mainly focus on the easy-axis anisotropic case with $I^z = 0.2$ unless otherwise noted, since it is well known that the easy-axis anisotropy favors the SkX in

centrosymmetric magnets[39–41,49,57]. We also focus on the case with $I^{\mathrm{BA}} > 0$, since qualitatively similar results are obtained for $I^{\mathrm{BA}} < 0$ by exchanging the x and y spin components.

The magnetic phase diagram of the model in Eq. (1) is obtained for the system size with $N = 96^2$ by carrying out simulated annealing in the following procedures. First, we start from a random spin configuration from high temperature $T_0 = 1.0$-10.0. Then, we reduce the temperature with the rate $T_{n+1} = \alpha T_n$, where T_n is the temperature in the nth step and $\alpha = 0.99995$-0.99999. At each temperature, we perform the standard Metropolis local updates in real space. The final temperature, which is typically taken at $T = 0.01$, is reached by spending totally 10^5-10^6 Monte Carlo sweeps. Finally, we perform 10^5-10^6 Monte Carlo sweeps for measurements at the final temperature, after 10^5-10^6 steps for thermalization. We also start the simulations from the spin patterns obtained at low temperatures to determine the phase boundaries between different magnetic states.

In order to identify each magnetic phase, we examine the spin and chirality configurations in the obtained states. The spin structure factor is given by

$$S_s^{\alpha}(\boldsymbol{q}) = \frac{1}{N} \sum_{j,l} S_j^{\alpha} S_l^{\alpha} e^{i\boldsymbol{q}\cdot(\boldsymbol{r}_j - \boldsymbol{r}_l)}, \tag{4}$$

with $\alpha = x, y, z$. For the in-plane component, we use the notation

$$S_s^{xy}(\boldsymbol{q}) = S_s^x(\boldsymbol{q}) + S_s^y(\boldsymbol{q}). \tag{5}$$

We also introduce the magnetic moments at $\boldsymbol{q}$ component as

$$m_{\boldsymbol{q}}^{\alpha} = \sqrt{\frac{S_s^{\alpha}(\boldsymbol{q})}{N}}. \tag{6}$$

In order to distinguish the in-plane components parallel and perpendicular to $\boldsymbol{Q}_1$ and $\boldsymbol{Q}_2$, we use local coordinate frames for the $\boldsymbol{Q}_1$ and $\boldsymbol{Q}_2$ components as

$$\boldsymbol{m}_{\boldsymbol{Q}_{\eta}} = (m_{\boldsymbol{Q}_{\eta}}^{\parallel}, m_{\boldsymbol{Q}_{\eta}}^{\perp}, m_{\boldsymbol{Q}_{\eta}}^z), \tag{7}$$

for $\eta = 1$ and 2, where $m_{\boldsymbol{Q}_{\eta}}^{\parallel}$ and $m_{\boldsymbol{Q}_{\eta}}^{\perp}$ are the in-plane parallel and perpendicular components, respectively. We also compute the net magnetization along the z direction

$$m_0 = \frac{1}{N} \sum_i S_i^z. \tag{8}$$

On the other hand, the scalar chirality χ_0 is evaluated by

$$\chi_0 = \left[\frac{1}{N} \sum_{i, \delta = \pm 1} \boldsymbol{S}_i \cdot (\boldsymbol{S}_{i+\delta\hat{x}} \times \boldsymbol{S}_{i+\delta\hat{y}}) \right]^2, \tag{9}$$

where $\hat{x}$ ($\hat{y}$) is the unit vector in the x (y) direction[20]. This quantity signals noncoplanarity of the spin structure. To distinguish the topology of each magnetic state, we also compute the skyrmion number defined by[58]

$$n_{\mathrm{sk}} = \frac{1}{2\pi N_m} \sum_{i, \delta = \pm 1} \tan^{-1} \frac{\boldsymbol{S}_i \cdot (\boldsymbol{S}_j \times \boldsymbol{S}_k)}{1 + \boldsymbol{S}_i \cdot \boldsymbol{S}_j + \boldsymbol{S}_j \cdot \boldsymbol{S}_k + \boldsymbol{S}_k \cdot \boldsymbol{S}_i}, \tag{10}$$
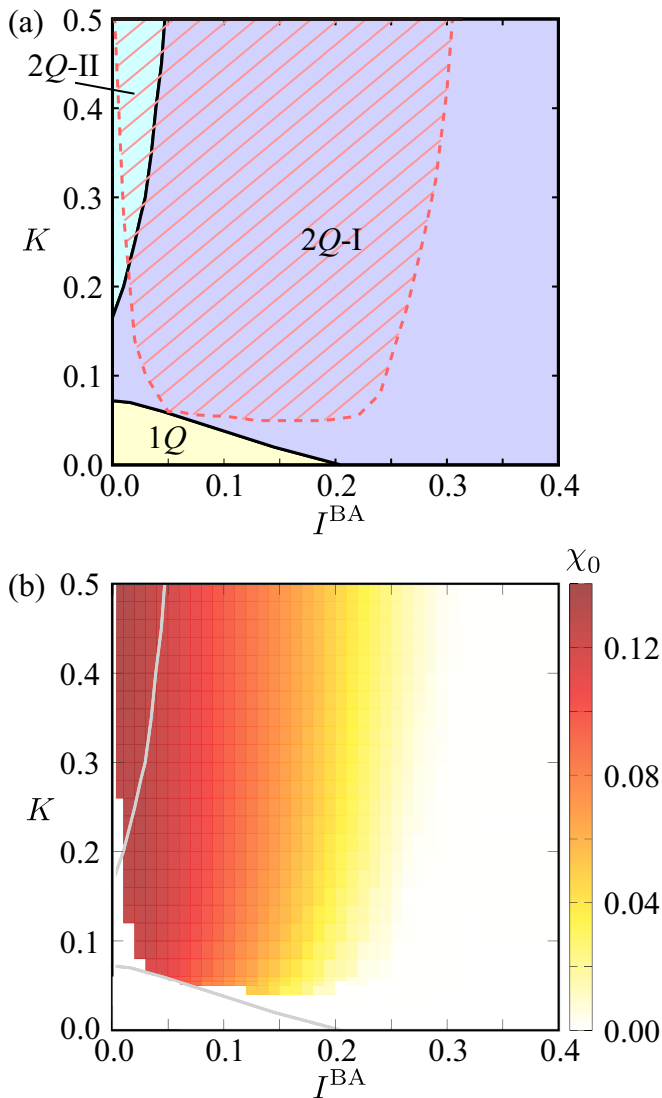
FIG. 1. (a) Magnetic phase diagram at zero magnetic field for $I^z = 0.2$ obtained by the simulated annealing down to $T = 0.01$. $2Q$-I and $2Q$-II stand for two different double-Q states, while $1Q$ is for the single-Q state. The hatched area shows the parameter region where the system undergoes a phase transition to a double-Q state with nonzero scalar chirality in an applied magnetic field, which is deduced to realize the SkX in the ground state. (b) Contour plot of the maximum value of χ_0 while varying H. The gray lines are the phase boundaries in (a).

where N_m is the number of magnetic unit cell in the system, and $j = i + \delta\hat{x}$ and $k = i + \delta\hat{y}$; the range of the arctangent is set as $[-\pi, \pi)$. n_{sk} is quantized at a nonzero value for topological spin textures, whereas χ_0 is not.

III. ZERO-FIELD PHASE DIAGRAM

First, we discuss the result in the absence of the magnetic field, $H = 0$. Figure 1(a) shows the magnetic phase diagram

while varying I^{BA} and K at $I^z = 0.2$ obtained by the simulated annealing down to $T = 0.01$. There are three magnetic phases, whose spin configurations in real space and the spin structure factors in momentum space are shown in Fig. 2. Note that each state is energetically degenerate with the one obtained by $90°$ degree rotation in the xy plane because of the fourfold rotational symmetry of the system. The three magnetic states do not have a net scalar chirality χ_0.

In the region for small I^{BA} and K, the single-Q ($1Q$) state is stabilized. At $I^{BA} = 0$, the $1Q$ state is characterized by an elliptical spiral in either the xz or yz plane. Reflecting the easy-axis anisotropy by I^z, the z component of the spin structure factor is larger than the xy component. A nonzero I^{BA} sets the spiral plane perpendicular to the ordering vector, i.e., the xz (yz) plane for the ordering vector $\boldsymbol{Q}_2$ ($\boldsymbol{Q}_1$); the state with $\boldsymbol{Q}_2$ is shown in Fig. 2(a). Thus, the $1Q$ state has an elliptical proper-screw spiral.

For larger I^{BA} and K, two types of the double-Q ($2Q$) state are realized. The $2Q$-I state occupies the largest portion of the phase diagram, adjacent to the $1Q$ state upon increasing I^{BA} and K in Fig. 1(a). The xy spin component is characterized by the double-Q peaks with different intensities, while the z spin component is characterized by the single-Q peak, as shown in the right two panels in Fig. 2(b). The real-space spin configuration in the left panel in Fig. 2(b) indicates that the spin texture in the $2Q$-I state is represented by a superposition of the proper-screw spiral along the $\boldsymbol{Q}_2$ direction and the sinusoidal wave along the $\boldsymbol{Q}_1$ direction. The double-Q structure in the xy spin component leads to a periodic array of vortices. Although this state does not have a net scalar chirality, it exhibits the chirality density wave along the $\boldsymbol{Q}_1$ direction[59–61].

For large K and small I^{BA}, the other double-Q state denoted as $2Q$-II appears in the phase diagram in Fig. 1(a). In this state, both xy and z components of the spin structure factor exhibit the single-Q peak at $\boldsymbol{Q}_2$ and $\boldsymbol{Q}_1$, respectively, as shown in Fig. 2(c). From the real-space spin structure, the spin pattern is represented by a superposition of the sinusoidal wave along the $\boldsymbol{Q}_1$ direction in the z-spin component and the cycloidal spiral along the $\boldsymbol{Q}_2$ direction in the xy-spin component. This state also exhibits the chirality density wave along the $\boldsymbol{Q}_1$ direction[59–61].

IV. SKYRMION CRYSTAL IN A FIELD

Next, we discuss the result in the presence of the magnetic field H. From the results obtained by the simulated annealing down to $T = 0.01$, we find that the system undergoes a phase transition to a double-Q state with nonzero scalar chirality χ_0 under the magnetic field in the hatched area in Fig. 1(a). The maximum value of χ_0 in the field is plotted in Fig. 1(b). As detailed later, the field-induced double-Q state is deduced to realize a square-type SkX in the ground state. The region spans both $2Q$-I and $2Q$-II states; we could not find the instability toward the SkX in the $1Q$ region.

In the following, we discuss the detailed changes of the spin textures for the magnetic field mainly in this region. Interestingly, the region is drastically extended down to the small
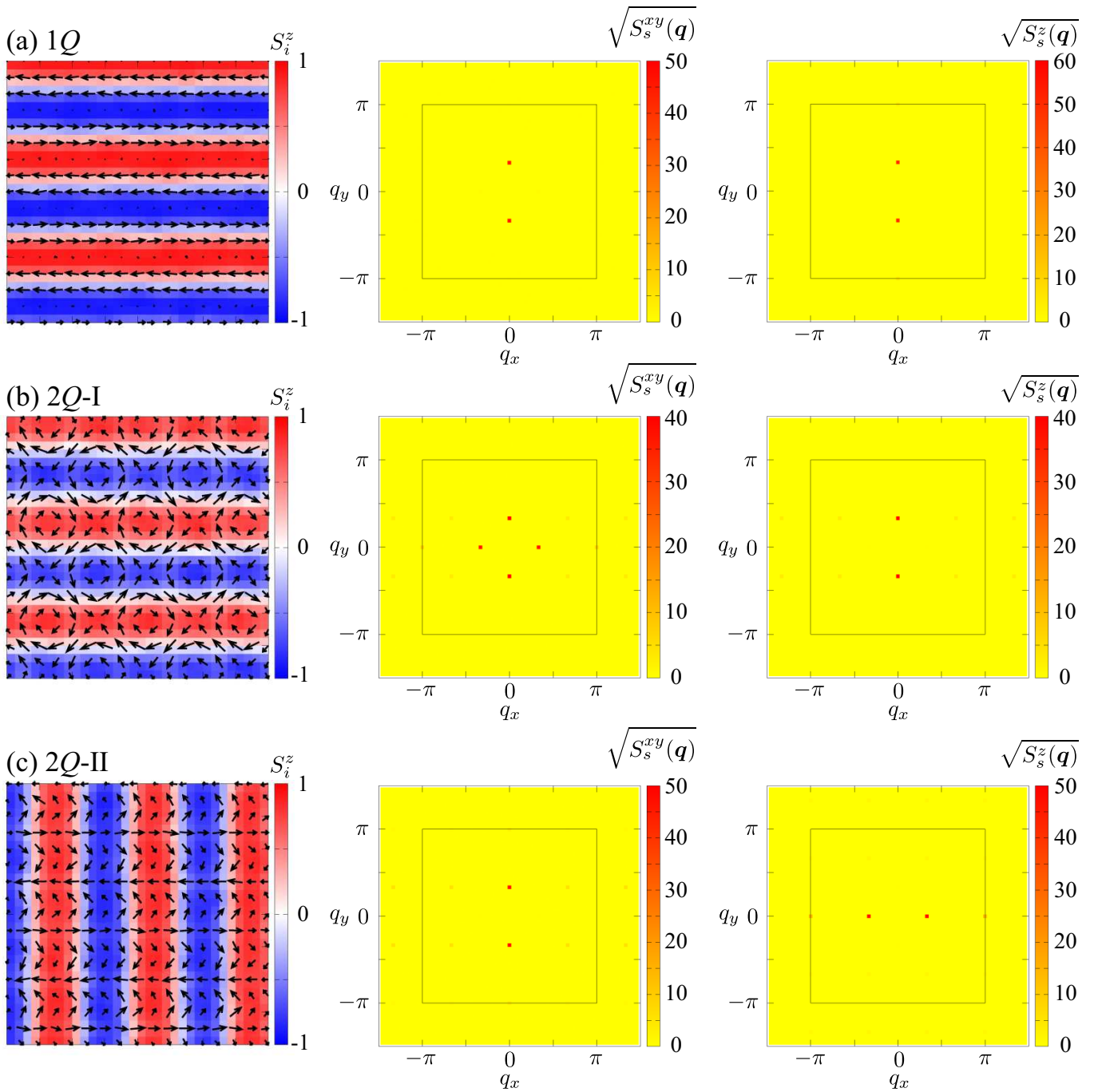
FIG. 2. (Left) Snapshots of the spin configurations in (a) the $1Q$ state for $K = 0.025$ and $I^{\mathrm{BA}} = 0.1$, (b) the $2Q$-I state for $K = 0.15$ and $I^{\mathrm{BA}} = 0.2$, and (c) the $2Q$-II state for $K = 0.5$ and $I^{\mathrm{BA}} = 0.04$. The arrows and the contour show the xy and z components of the spin moment, respectively. (Middle and right) The square root of the xy and z components of the spin structure factor, respectively. The black solid squares represent the first Brillouin zone.

K region by introducing I^{BA}; it is limited to $K \gtrsim 0.58$ at $I^{\mathrm{BA}} = 0$ (not shown), whereas the boundary comes down to $K \simeq 0.07$ for $I^{\mathrm{BA}} \simeq 0.05$. This indicates the importance of the bond-dependent anisotropic interaction I^{BA} for the stabilization of the square SkX. We show the result while changing I^{BA} in Sec. IV A. Then, we discuss the effects of

the biquadratic interaction K in Sec. IV B and the easy-axis anisotropic interaction I^z in Sec. IV C. In these sections, we mainly focus on the region where the $2Q$-I state is stable at zero field, which appears to be relevant to the experiment in GdRu$_2$Si$_2$ as discussed in Sec. V A; the $2Q$-II region with smaller I^{BA} and larger K is discussed in Appendix A.
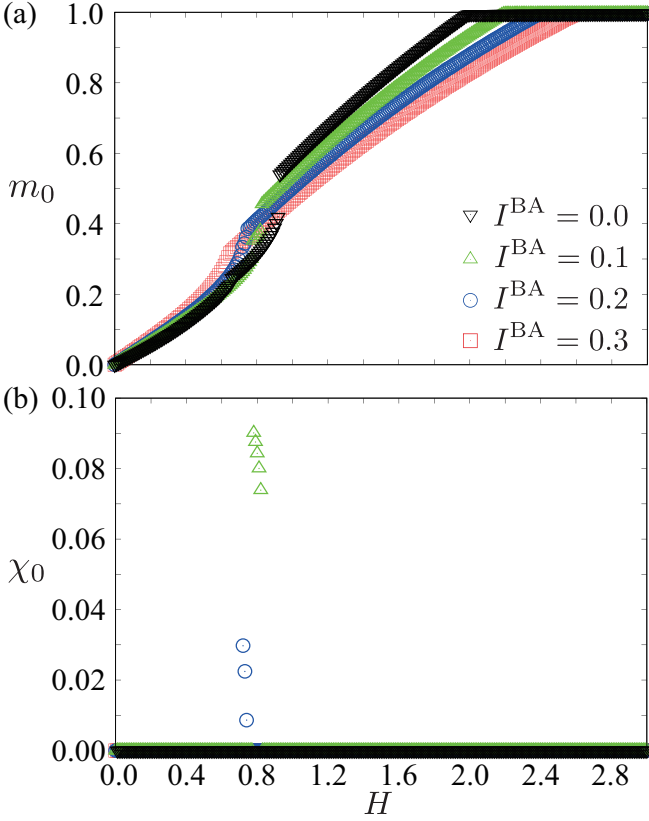
FIG. 3. H dependence of (a) m_0 and (b) χ_0 for $I^{\mathrm{BA}} = 0$, 0.1, 0.2, and 0.3 at $K = 0.2$ and $I^z = 0.2$.

A. Effect of bond-dependent anisotropic interaction

Figures 3 and 4 show the magnetic field dependence of the spin- and chirality-related quantities for several values of I^{BA} at $K = 0.2$ and $I^z = 0.2$. In the simulations, as in the case of zero field, energetically-degenerate magnetic states are obtained from different initial configurations owing to the fourfold rotational symmetry; e.g., the single-Q state with $\boldsymbol{m}_{\boldsymbol{Q}_1} \neq 0$ is equivalent to that with $\boldsymbol{m}_{\boldsymbol{Q}_2} \neq 0$. For better readability, we show the spin texture in each ordered state by appropriately sorting $(\boldsymbol{m}_{\boldsymbol{Q}_\nu})^2$ in Fig. 4 and hereafter.

At $I^{\mathrm{BA}} = 0$, where the 2Q-II state is stabilized at $H = 0$, the dominant $(m_{\boldsymbol{Q}_2}^z)^2$ is suppressed and the subdominant $(m_{\boldsymbol{Q}_1}^{\parallel})^2$ and $(m_{\boldsymbol{Q}_1}^{\perp})^2$ are enhanced while increasing H, as shown in Fig. 4(a). In the narrow range of $0.60 \lesssim H \lesssim 0.65$, a different double-$Q$ (2Q-III) state is stabilized, whose real-space spin configuration and spin structure factor are shown in Fig. 5(a). Compared to the 2Q-II state, the 2Q-III state has additional magnetic moments in $(m_{\boldsymbol{Q}_1}^z)^2$, $(m_{\boldsymbol{Q}_2}^{\parallel})^2$, and $(m_{\boldsymbol{Q}_2}^{\perp})^2$, as shown in Fig. 4(a). The net magnetization m_0 shows a small anomaly corresponding to the appearance of the 2Q-III state, as shown in Fig. 3(a). Upon further increasing H, the 2Q-II state appears again for $H \gtrsim 0.65$, which turns into the single-Q conical spiral state at $H \simeq 0.93$ with a jump of m_0, as shown in Figs. 3(a) and 4(a). The single-Q conical state
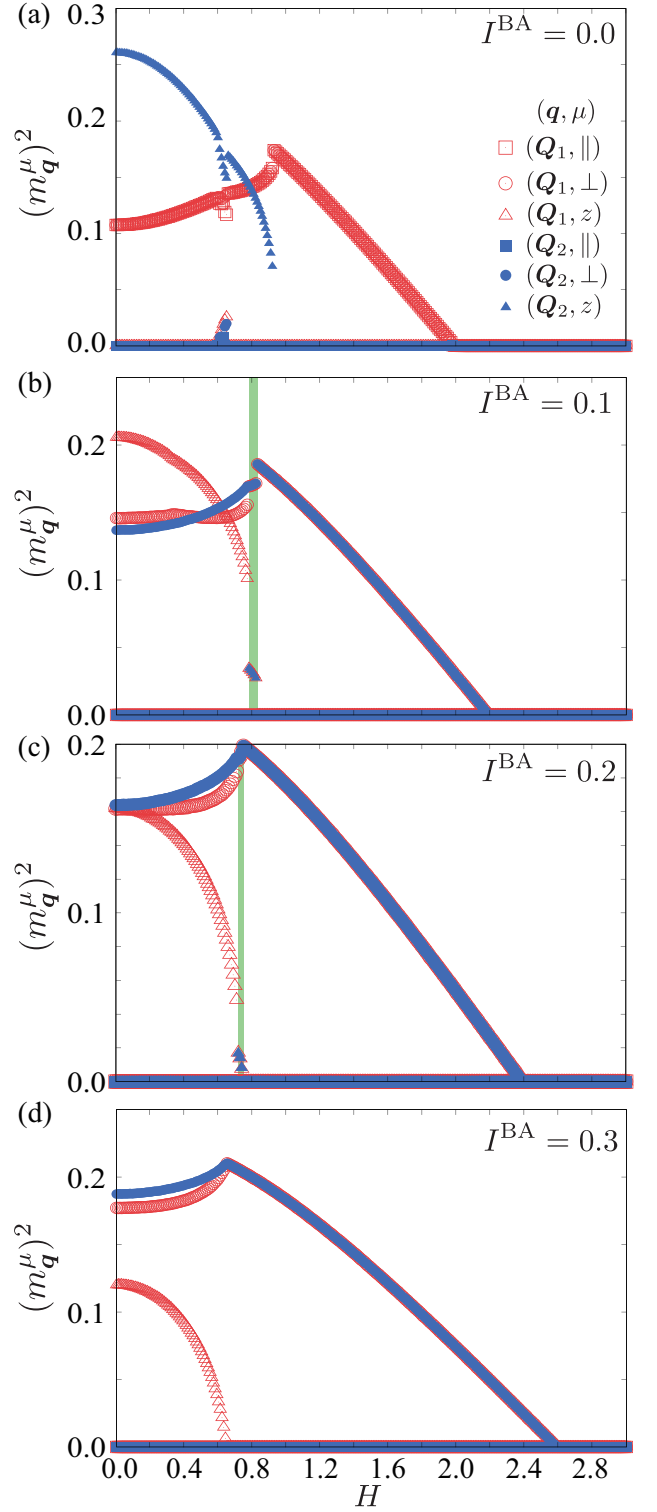

FIG. 4. (a)-(d) $(m_{\boldsymbol{q}}^\mu)^2$ ($\mu = \parallel, \perp, z$ and $\boldsymbol{q} = \boldsymbol{Q}_1, \boldsymbol{Q}_2$) for (a) $I^{\mathrm{BA}} = 0$, (b) $I^{\mathrm{BA}} = 0.1$, (c) $I^{\mathrm{BA}} = 0.2$, and (d) $I^{\mathrm{BA}} = 0.3$ at $K = 0.2$ and $I^z = 0.2$. The green regions in (b) and (c) indicate the states with nonzero χ_0.

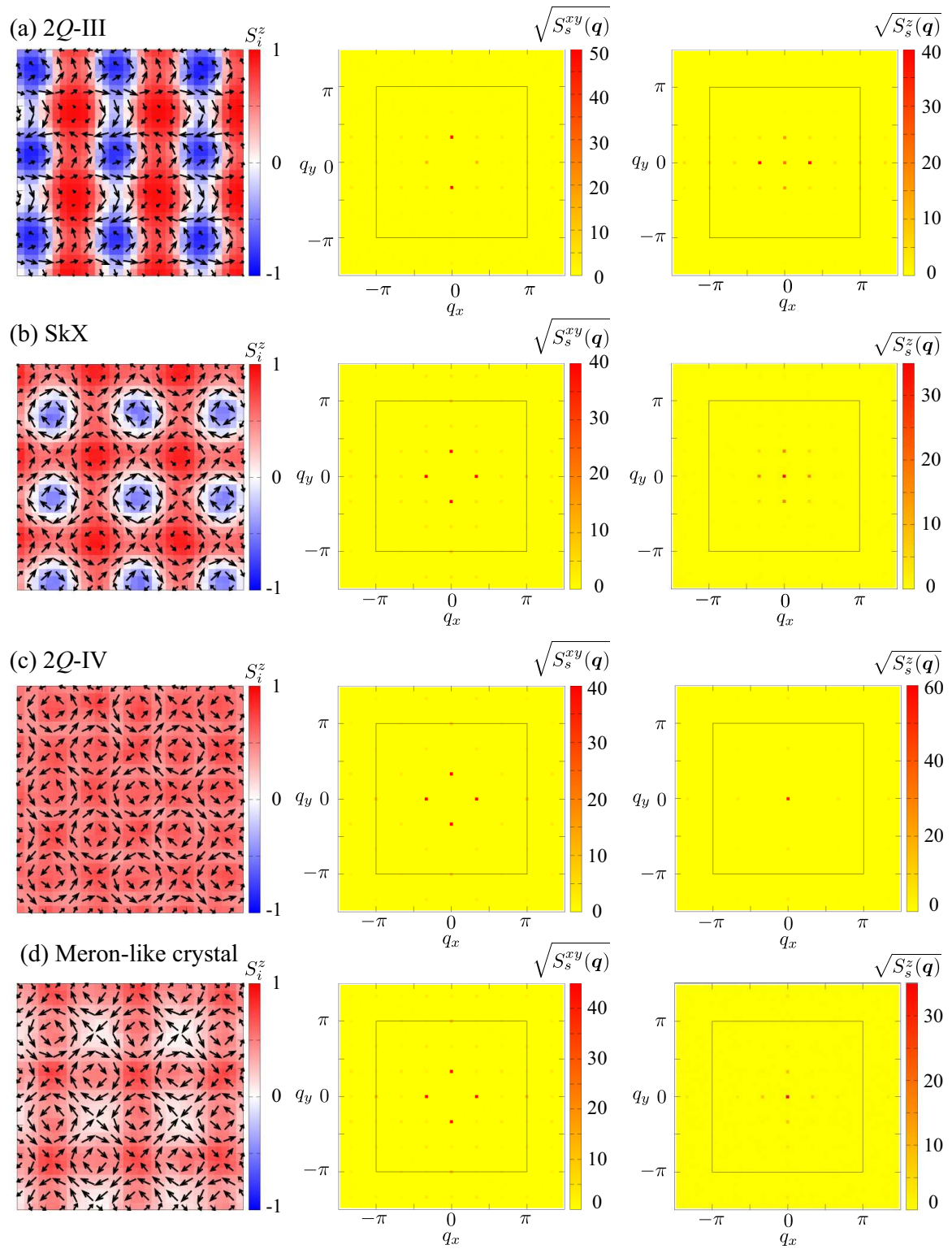continuously changes into the fully-polarized state at $H \simeq 2$.

FIG. 5. (Left) Snapshots of the spin configurations in (a) the 2Q-III state for $I^{\mathrm{BA}} = 0$ and $H = 0.65$, (b) the SkX for $I^{\mathrm{BA}} = 0.1$ and $H = 0.78$, (c) the 2Q-IV state for $I^{\mathrm{BA}} = 0.1$ and $H = 1$, and (d) the meron-like crystal for $I^{\mathrm{BA}} = 0.2$ and $H = 0.74$ at $K = 0.2$. The arrows and the contour show the xy and z components of the spin moment, respectively. (Middle and right) The square root of the xy and z components of the spin structure factor, respectively. The black solid squares represent the first Brillouin zone.

Throughout all these spin states, χ_0 is always zero, as shown   in Fig. 3(b) (see also Fig. 1(b)).

For $I^{\mathrm{BA}} = 0.1$ and 0.2, however, we find another double-Q state with nonzero χ_0 in a magnetic field. In both cases, we obtain three double-Q states in addition to the fully-polarized state, as shown in Figs. 4(b) and 4(c). The low-field state corresponds to the 2Q-I state connected to that at $H = 0$ [see Fig. 2(b)], while the high-field state before entering the fully-polarized state corresponds to a different double-Q (2Q-IV) state, whose spin structure is shown in Fig. 5(c). This 2Q-IV state exhibits the double-Q peaks at $(m_{\boldsymbol{Q}_1}^{\perp})^2$ and $(m_{\boldsymbol{Q}_2}^{\perp})^2$ in addition to the uniform magnetization. In other words, this state is characterized by a superposition of two sinusoidal waves along the $\boldsymbol{Q}_1$ and $\boldsymbol{Q}_2$ directions. We note that a similar spin texture was also obtained even without I^{BA} by considering large K[46].

The intermediate-field state, which is sandwiched by the 2Q-I and 2Q-IV states, shows nonzero χ_0, as shown in Fig. 3(b). The phase transitions between these three double-Q states are of first order with discontinuities in χ_0 as well as m_0. The spin structure of the intermediate state in the case of $I^{\mathrm{BA}} = 0.1$ is shown in Fig. 5(b). It is a square-type SkX with fourfold rotational symmetry, composed of the equal weights for $\boldsymbol{Q}_1$ and $\boldsymbol{Q}_2$ in both xy- and z-spin components. Indeed, we find that the skyrmion number n_{sk} in Eq. (10) for this state asymptotically approaches ± 1 while lowering temperature (not shown). Note that the SkX is energetically degenerate with the anti-skyrmion counterpart in the present model; the degeneracy can be lifted by including contributions from higher harmonics, as discussed in Ref. 62.

The results are overall similar for $I^{\mathrm{BA}} = 0.2$, as shown in Figs. 3 and 4(c). We note, however, that the field range of the intermediate double-Q state becomes narrow and χ_0 is reduced compared with those for $I^{\mathrm{BA}} = 0.1$, since I^{BA} tends to forces the spins to lie in a plane; actually, $|n_{\mathrm{sk}}|$ obtained at $T = 0.01$ decreases while increasing I^{BA} in the hatched region in Fig. 1(a) (not shown). In the present simulation for $I^{\mathrm{BA}} = 0.2$, the intermediate state with nonzero χ_0 has a nonzero value of $|n_{\mathrm{sk}}|$ close to 1 in the region close to the phase boundary with the lower-field 2Q-I state, but it is reduced to less than 0.5 when approaching the phase boundary with the higher-field 2Q-IV state. Interestingly, the spin configuration with the reduced $|n_{\mathrm{sk}}|$ less than 0.5 is characterized by the meron-crystal-like one as shown in Fig. 5(d), which has a periodic swirling spin texture as the SkX but all the spins have positive z-spin moments[49,63–66].

The results with non-quantized n_{sk} indicate that the temperature in our simulated annealing is not sufficiently low to reach the ground state. From the temperature dependence of n_{sk}, however, we conclude that the system exhibits the square-type SkX with $n_{\mathrm{sk}} = \pm 1$ in most of the hatched region in Fig. 1(a) except for a narrow window with large I^{BA}. For instance, the window ranges for $0.25 \lesssim I^{\mathrm{BA}} \lesssim 0.27$ at $K = 0.2$. In the narrow window, there are, at least, three possibilities for the fate of the system in the low-temperature limit: a SkX with $n_{\mathrm{sk}} = \pm 1$, a meron crystal with $n_{\mathrm{sk}} = \pm 1/2$, and a topologically trivial double-Q state with nonzero χ_0 but vanishing n_{sk}. We may have successive phase transitions among these states, while changing the magnetic field and temperature. To clarify this subtle issue, we need further studies at

lower temperature, which are computationally laborious.

When increasing I^{BA} outside the hatched region in Fig. 1(a), the intermediate state with nonzero χ_0 vanishes, as exemplified for $I^{\mathrm{BA}} = 0.3$ in Figs. 3 and 4(d). In this case, the 2Q-I state continuously changes into the 2Q-IV state.
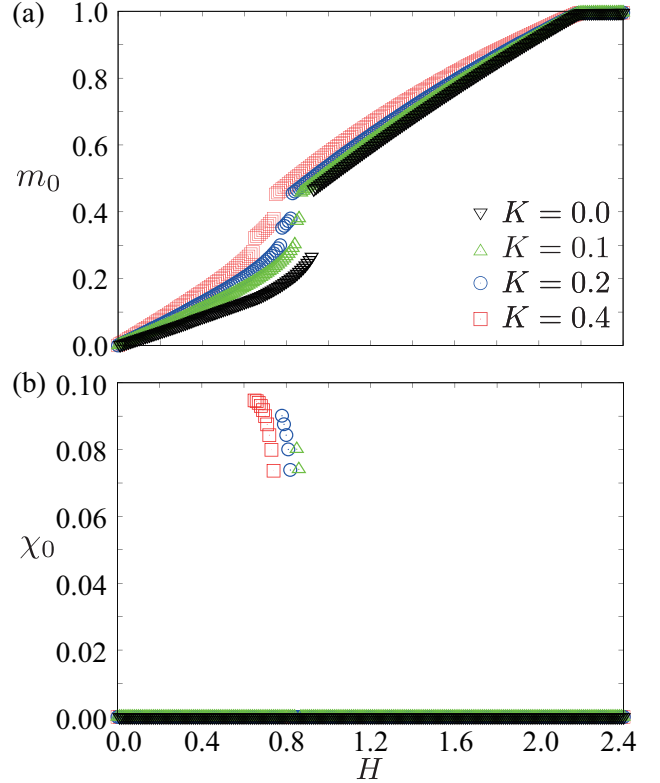

FIG. 6. H dependence of (a) m_0 and (b) χ_0 for $K = 0, 0.1, 0.2$, and 0.4 at $I^{\mathrm{BA}} = 0.1$ and $I^z = 0.2$.

B. Effect of biquadratic interaction

Next, we discuss the behavior while changing K. Figures 6 and 7 show the magnetic field dependence of the spin- and chirality-related quantities for $K = 0, 0.1, 0.2$, and 0.4 at $I^{\mathrm{BA}} = 0.1$ and $I^z = 0.2$. At $K = 0$, the 1Q state is stabilized at $H = 0$, as shown in Fig. 1(a). While increasing H, the 1Q state continuously turns into the 2Q-I state at $H \simeq 0.68$, and then, there is a first-order phase transition to the 2Q-IV state at $H \simeq 0.93$, as shown in Fig. 7(a). The 2Q-IV state changes into the fully-polarized state at $H \simeq 2.2$. m_0 shows a jump at the transition from 2Q-I to 2Q-IV, as shown in Fig. 6(a). χ_0 is always zero as shown in Fig. 6(b).

Meanwhile, for $K = 0.1, 0.2$, and 0.4, where the 2Q-I state is stabilized at zero field as shown in Fig. 1(a), the square SkX phase appears in the intermediate-field region. The phase sequence while increasing H is similar to those in Sec. IV A, namely, from 2Q-I, SkX, 2Q-IV, and finally to the fully-polarized state, as shown in Fig. 7(b) for $K = 0.1$, Fig. 4(b) for $K = 0.2$, and Fig. 7(c) for $K = 0.4$. The emer-
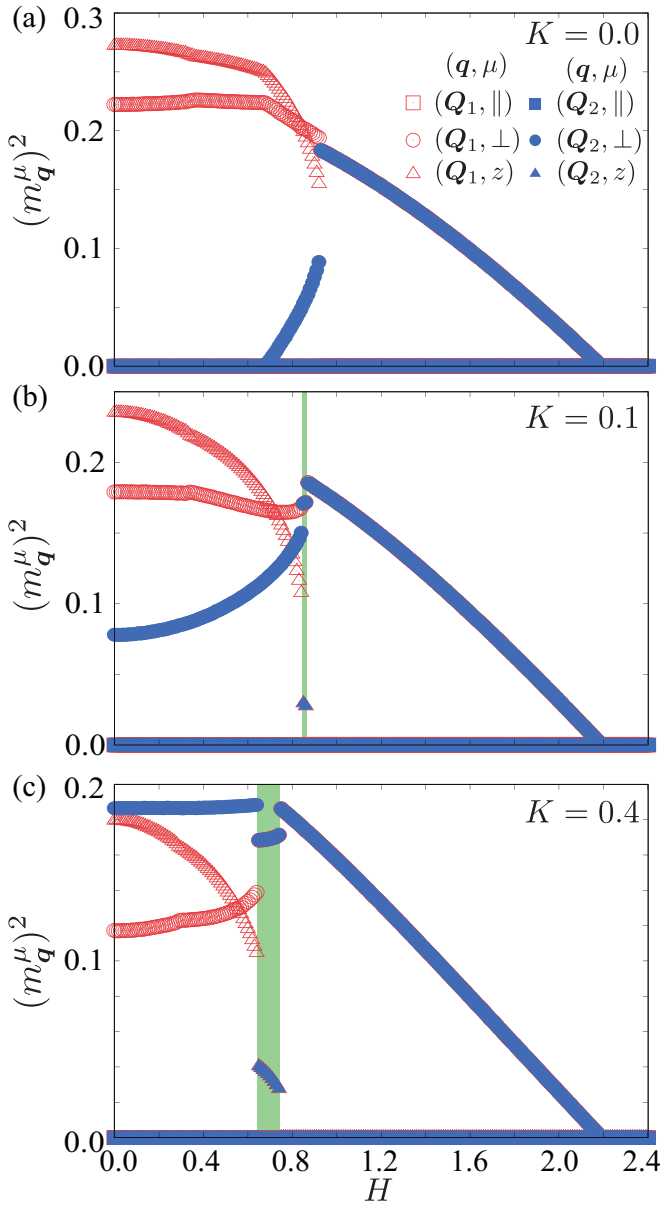
FIG. 7. (a)-(c) $(m_{\boldsymbol{q}}^{\mu})^2$ ($\mu = \|, \perp, z$ and $\boldsymbol{q} = \boldsymbol{Q}_1, \boldsymbol{Q}_2$) for (a) $K = 0$, (b) $K = 0.1$, and (c) $K = 0.4$ at $I^{\mathrm{BA}} = 0.1$ and $I^z = 0.2$. The result at $K = 0.2$ is shown in Fig. 4(b). The green regions in (b) and (c) indicate the states with nonzero χ_0.

FIG. 8. H dependence of (a) m_0 and (b) χ_0 for $I^z = -0.05$, 0, 0.1, and 0.2 at $I^{\mathrm{BA}} = 0.05$ and $K = 0.2$.

C. Effect of easy-axis anisotropic interaction

Lastly, we investigate the effect of I^z on the SkX by considering the parameter region where the SkX is relatively robust, i.e., in the small I^{BA} region. We show the results at $I^{\mathrm{BA}} = 0.05$ and $K = 0.2$ while decreasing I^z from 0.2 to 0 in Figs. 8 and 9. While decreasing I^z, the region for the SkX becomes narrower. For $I^z = 0$, χ_0 retains a tiny nonzero value only at $H \simeq 0.58$, as shown in Figs. 8(b). In the present simulation at $T = 0.01$, this state exhibits a nonzero absolute value of n_{sk} less than 0.5, whose spin texture is similar to that in the meron-like crystal shown in Fig. 5(d). By introducing the easy-plane anisotropic interaction with $I^z = -0.05$, the region with nonzero χ_0 vanishes as shown in Fig. 9(d). The results clearly indicate that the easy-axis anisotropic interaction plays an important role in the stabilization of the SkX. This tendency is commonly seen in centrosymmetric systems on a triangular lattice[39–41,57].

gence of the SkX is signaled by nonzero χ_0 in Fig. 6(b) as well as the jumps in m_0 in Fig. 6(a). The maximum value of χ_0 becomes larger for larger K, as shown in Fig. 6(b). At the same time, the field range of the SkX state also becomes wider for larger K. These indicate that the biquadratic interaction K originating from the itinerant nature of electrons plays an important role in the stabilization of the SkX, as in the previous studies[46,47,49,67].
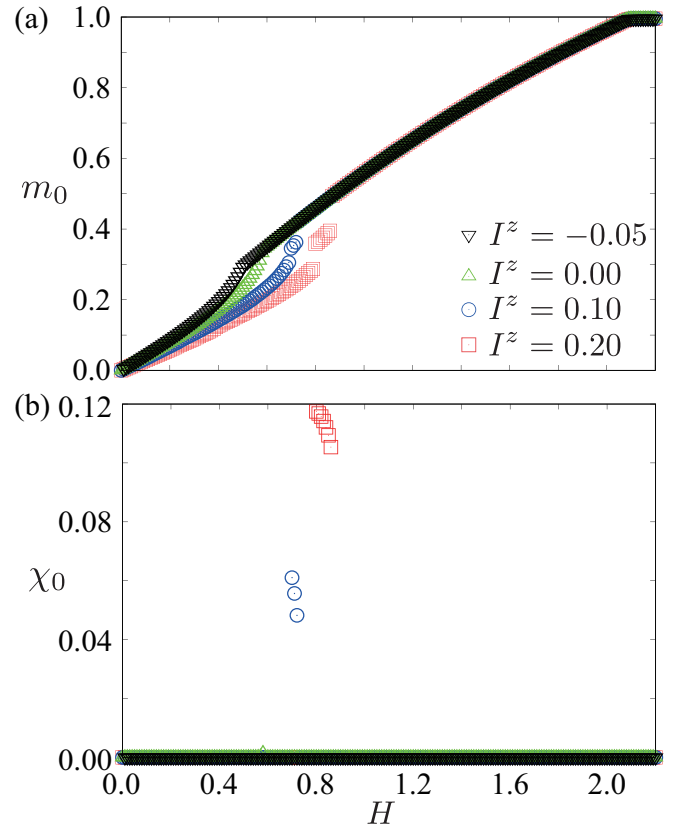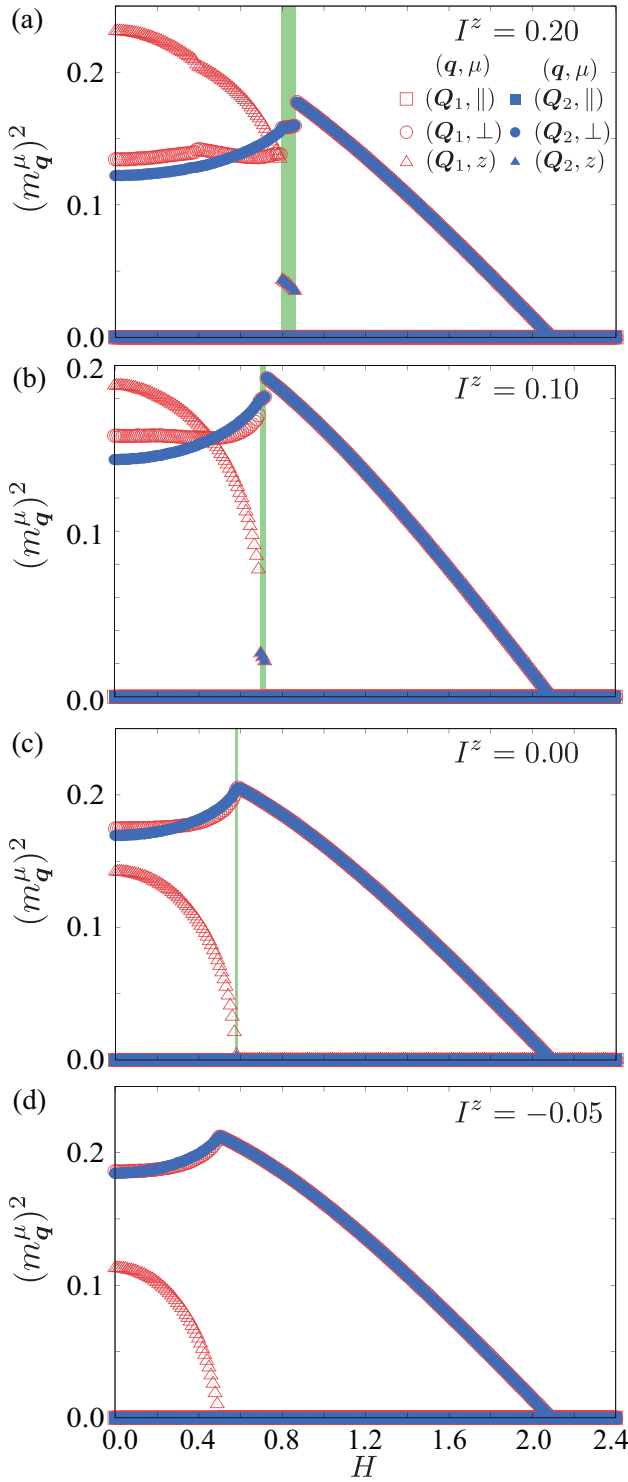
FIG. 9. (a)-(d) $(m_{\boldsymbol{q}}^{\mu})^2$ ($\mu = \parallel, \perp, z$ and $\boldsymbol{q} = \boldsymbol{Q}_1, \boldsymbol{Q}_2$) for (a) $I^z = 0.2$, (b) $I^z = 0.1$, (c) $I^z = 0$, and (d) $I^z = -0.05$ at $I^{\mathrm{BA}} = 0.05$ and $K = 0.2$. The green regions in (a), (b), and (c) indicate the states with nonzero χ_0.

V. DISCUSSION

A. Comparison with experiment

Let us compare our results with the recent experiments for a centrosymmetric material GdRu$_2$Si$_2$ where the square SkX was discovered in the magnetic field[36,37]. In GdRu$_2$Si$_2$, three distinct phases were observed besides the fully-polarized state at high fields, which were denoted as Phase I, II, and III from the low to high magnetic field[36,37]. Phase I has an anisotropic double-Q structure, while Phase II and III show isotropic double-Q structures. Among the three, Phase II shows a large topological Hall effect, and was identified as the square SkX by the Lorentz transmission electron microscopy[36]. The resonant x-ray scattering and the subsequent spectroscopic-imaging scanning tunneling microscopy measurements implied that the spin textures in Phase I and III were characterized by a superposition of the modulated screw and the fan structure, respectively[36,37].

Our effective spin model exhibits the square SkX in the intermediate-field region similar to Phase II in GdRu$_2$Si$_2$. The SkX appears in a wide parameter region of I^{BA} and K for $I^z > 0$. Furthermore, we obtain two different types of double-Q states, the 2Q-I and 2Q-IV states, in the lower- and higher-field regions of the SkX, which possess similar features to Phase I and III in GdRu$_2$Si$_2$, respectively; the low-field 2Q-I state shows the modulated screw structure consisting of the proper-screw spiral and the sinusoidal wave as shown in Fig. 2(b), and the high-field 2Q-IV state shows the fan structure consisting of the sinusoidal waves and the uniform magnetization as shown in Fig. 5(c). These results indicate good agreement between Phase I, II, and III in GdRu$_2$Si$_2$ and the 2Q-I, SkX, and 2Q-IV states in our model.

Moreover, our model analysis explains the stability of the square SkX against the other phases semiquantitatively. In GdRu$_2$Si$_2$, the square SkX was observed in a narrow field range between 2.1 T and 2.5 T, where the saturation field is around 10 T[36]. Thus, the ratio of the magnetic field range where the square SkX is stabilized to the saturation field is about 4%. On the other hand, the ratio in the present model ranges is typically a few percent of the saturation field as shown in Sec. IV, which is consistent with the experimental value.

From these observations, we conclude that our model describes the essential physics in the centrosymmetric skyrmion material GdRu$_2$Si$_2$. Our results clearly indicate that the synergy between the biquadratic interaction arising from the itinerant nature of electrons, the bond-dependent anisotropic interaction, and the easy-axis anisotropic interaction plays a central role in the skyrmion physics in this compound.

B. Comparison with the triangular skyrmion crystal

Let us compare the stability between the square and triangular SkXs in centrosymmetric itinerant electron systems. The triangular SkX on a triangular lattice is stabilized by taking into account either the positive biquadratic[46], the bond-

dependent anisotropic[68,69], or the easy-axis anisotropic inter-action[70]. In other words, it can be stabilized by only one of the three interactions. In stark contrast, as shown in the present study, the interplay among the three interactions is essential to realize the square SkX on a square lattice. Furthermore, the square SkX on a centrosymmetric lattice system has not been reported by other mechanisms thus far, in contrast to the triangular ones being realized, e.g., by frustrated exchange interactions[38–42]. Thus, the present square SkX is characteristic of itinerant magnets with magnetic anisotropy, which strongly suggests that the SkX observed in GdRu$_2$Si$_2$ is generated as a consequence of such a synergetic effect.

VI. SUMMARY

We have investigated the stability of the square SkX on a centrosymmetric tetragonal lattice in itinerant magnets. Our results were obtained by numerically simulated annealing for an effective spin model with the long-ranged anisotropic interactions defined in momentum space. We found that the square SkX is stabilized by the interplay among the positive biquadratic, bond-dependent anisotropic, and easy-axis anisotropic interactions in an external magnetic field. The square SkX is a double-Q state composed of two helices with equal weight, retaining the fourfold rotational symmetry of the square lattice. In addition, we found several different double-Q states around the SkX. We showed that the SkX becomes more stable for larger biquadratic interaction, smaller but nonzero bond-dependent anisotropic interaction, and larger easy-axis anisotropic interaction. Our results well reproduce the three magnetic phases including the square SkX observed in GdRu$_2$Si$_2$ in the magnetic field[36,37], indicating the importance of the synergetic effect between the three interactions in this material. Our systematic study would be a reference to further exploration of skyrmion-hosting materials in centrosymmetric itinerant magnets.

Appendix A: Effect of magnetic field on $2Q$-II state

In this Appendix, we show the effect of the magnetic field on the $2Q$-II state within the hatched region in Fig. 1(a). We show that the square SkX is induced also in this region by the magnetic field. Figure 10 shows the result at $I^{\mathrm{BA}} = 0.02$ for $K = 0.4$ and $I^z = 0.2$. In contrasts to the result in Fig. 4(a) for $I^{\mathrm{BA}} = 0$ and $K = 0.2$, which is also the $2Q$-II state at zero field, there appear four states in addition to the fully-

polarized state for $H \gtrsim 2$: the $2Q$-II state for $0 \lesssim H \lesssim 0.44$, the $2Q$-III state for $0.44 \lesssim H \lesssim 0.71$, the square SkX for $0.71 \lesssim H \lesssim 0.82$, and the $2Q$-IV state for $0.82 \lesssim H \lesssim 2$, as shown in Fig. 10(b). Their phase transitions are signaled by the kinks in m_0 around $H \simeq 0.44$ and $H \simeq 2$ and the jumps in m_0 and χ_0 at $H \simeq 0.71$ and $H \simeq 0.82$, as shown in Fig. 10(a).
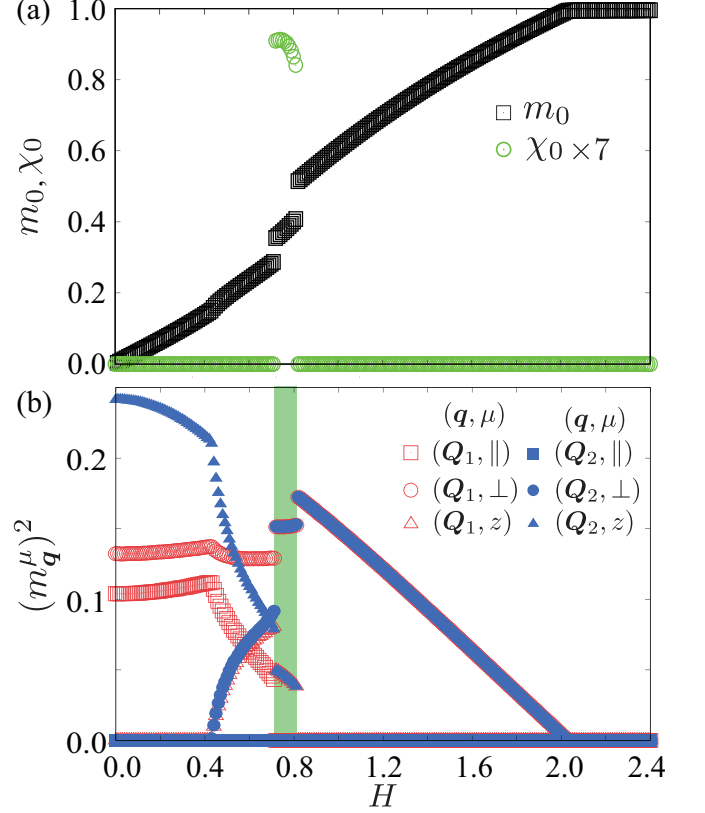

FIG. 10. H dependence of (a) m_0 and χ_0 and (b) $(m_q^\mu)^2$ ($\mu = \|, \perp, z$ and $q = Q_1, Q_2$) for $I^{\mathrm{BA}} = 0.02$ at $K = 0.4$ and $I^z = 0.2$. The green region in (b) indicates the states with nonzero χ_0.

[1] A. N. Bogdanov and D. A. Yablonskii, *Thermodynamically stable "vortices" in magnetically ordered crystals: The mixed state of magnets*, Sov. Phys. JETP **68**, 101 (1989).

[2] A. Bogdanov and A. Hubert, *Thermodynamically stable magnetic vortex states in magnetic crystals*, J. Magn. Magn. Mater. **138**, 255 (1994).

[3] U. K. Rößler, A. N. Bogdanov, and C. Pfleiderer, *Spontaneous skyrmion ground states in magnetic metals*, Nature **442**, 797 (2006).

[4] S. Mühlbauer, B. Binz, F. Jonietz, C. Pfleiderer, A. Rosch, A. Neubauer, R. Georgii, and P. Böni, *Skyrmion lattice in a chiral magnet*, Science **323**, 915 (2009).

[5] X. Z. Yu, Y. Onose, N. Kanazawa, J. H. Park, J. H. Han, Y. Matsui, N. Nagaosa, and Y. Tokura, *Real-space observation of a two-dimensional skyrmion crystal*, Nature **465**, 901 (2010).

[6] N. Nagaosa and Y. Tokura, *Topological properties and dynamics of magnetic skyrmions*, Nat. Nanotech. **8**, 899 (2013).

[7] A. Fert, N. Reyren, and V. Cros, *Magnetic skyrmions: advances in physics and potential applications*, Nat. Rev. Mater. **2**, 17031 (2017).

[8] P. Bruno, V. K. Dugaev, and M. Taillefumier, *Topological Hall Effect and Berry Phase in Magnetic Nanostructures*, Phys. Rev. Lett. **93**, 096806 (2004).

[9] A. Neubauer, C. Pfleiderer, B. Binz, A. Rosch, R. Ritz, P. G. Niklowitz, and P. Böni, *Topological Hall Effect in the A Phase of MnSi*, Phys. Rev. Lett. **102**, 186602 (2009).

[10] N. Kanazawa, Y. Onose, T. Arima, D. Okuyama, K. Ohoyama, S. Wakimoto, K. Kakurai, S. Ishiwata, and Y. Tokura, *Large Topological Hall Effect in a Short-Period Helimagnet MnGe*, Phys. Rev. Lett. **106**, 156603 (2011).

[11] Y. Shiomi, N. Kanazawa, K. Shibata, Y. Onose, and Y. Tokura, *Topological Nernst effect in a three-dimensional skyrmion-lattice phase*, Phys. Rev. B **88**, 064409 (2013).

[12] Y. P. Mizuta and F. Ishii, *Large anomalous Nernst effect in a skyrmion crystal*, Sci. Rep. **6**, 28076 (2016).

[13] K. Hamamoto, M. Ezawa, K. W. Kim, T. Morimoto, and N. Nagaosa, *Nonlinear spin current generation in noncentrosymmetric spin-orbit coupled systems*, Phys. Rev. B **95**, 224430 (2017).

[14] S. Seki, M. Garst, J. Waizner, R. Takagi, N. Khanh, Y. Okamura, K. Kondou, F. Kagawa, Y. Otani, and Y. Tokura, *Propagation dynamics of spin excitations along skyrmion strings*, Nat. Commun. **11**, 1 (2020).

[15] M. V. Berry, *Quantal phase factors accompanying adiabatic changes*, Proceedings of the Royal Society of London A: Mathematical, Physical and Engineering Sciences **392**, 45 (1984).

[16] D. Loss and P. M. Goldbart, *Persistent currents from Berry's phase in mesoscopic systems*, Phys. Rev. B **45**, 13544 (1992).

[17] D. Xiao, M.-C. Chang, and Q. Niu, *Berry phase effects on electronic properties*, Rev. Mod. Phys. **82**, 1959 (2010).

[18] A. Fert, V. Cros, and J. Sampaio, *Skyrmions on the track*, Nat. Nanotechnol. **8**, 152 (2013).

[19] N. Romming, C. Hanneken, M. Menzel, J. E. Bickel, B. Wolter, K. von Bergmann, A. Kubetzka, and R. Wiesendanger, *Writing and deleting single magnetic skyrmions*, Science **341**, 636 (2013).

[20] S. D. Yi, S. Onoda, N. Nagaosa, and J. H. Han, *Skyrmions and anomalous Hall effect in a Dzyaloshinskii-Moriya spiral magnet*, Phys. Rev. B **80**, 054416 (2009).

[21] M. Mochizuki, *Spin-Wave Modes and Their Intense Excitation Effects in Skyrmion Crystals*, Phys. Rev. Lett. **108**, 017601 (2012).

[22] W. Münzer, A. Neubauer, T. Adams, S. Mühlbauer, C. Franz, F. Jonietz, R. Georgii, P. Böni, B. Pedersen, M. Schmidt, A. Rosch, and C. Pfleiderer, *Skyrmion lattice in the doped semiconductor $Fe_{1-x}Co_xSi$*, Phys. Rev. B **81**, 041203 (2010).

[23] S. Seki, X. Z. Yu, S. Ishiwata, and Y. Tokura, *Observation of skyrmions in a multiferroic material*, Science **336**, 198 (2012).

[24] I. Kézsmárki, S. Bordács, P. Milde, E. Neuber, L. M. Eng, J. S. White, H. M. Rønnow, C. D. Dewhurst, M. Mochizuki, K. Yanai, H. Nakamura, D. Ehlers, V. Tsurkan, and A. Loidl, *Neel-type skyrmion lattice with confined orientation in the polar magnetic semiconductor GaV_4S_8*, Nat. Mater. **14**, 1116 (2015).

[25] J. T. Lee, J. Chess, S. Montoya, X. Shi, N. Tamura, S. Mishra, P. Fischer, B. McMorran, S. Sinha, E. Fullerton, *et al.*, *Synthesizing skyrmion bound pairs in Fe-Gd thin films*, Appl. Phys. Lett.

109, 022402 (2016).

[26] S. Woo, K. Litzius, B. Krüger, M.-Y. Im, L. Caretta, K. Richter, M. Mann, A. Krone, R. M. Reeve, M. Weigand, *et al.*, *Observation of room-temperature magnetic skyrmions and their current-driven dynamics in ultrathin metallic ferromagnets*, Nat. Mater. **15**, 501 (2016).

[27] A. Soumyanarayanan, M. Raju, A. G. Oyarce, A. K. Tan, M.-Y. Im, A. P. Petrović, P. Ho, K. Khoo, M. Tran, C. Gan, *et al.*, *Tunable room-temperature magnetic skyrmions in Ir/Fe/Co/Pt multilayers*, Nat. Mater. **16**, 898 (2017).

[28] R. Takagi, X. Z. Yu, J. S. White, K. Shibata, Y. Kaneko, G. Tatara, H. M. Rønnow, Y. Tokura, and S. Seki, *Low-Field Bi-Skyrmion Formation in a Noncentrosymmetric Chimney Ladder Ferromagnet*, Phys. Rev. Lett. **120**, 037203 (2018).

[29] S. Sen, C. Singh, P. K. Mukharjee, R. Nath, and A. K. Nayak, *Observation of the topological Hall effect and signature of room-temperature antiskyrmions in Mn-Ni-Ga D_{2d} Heusler magnets*, Phys. Rev. B **99**, 134404 (2019).

[30] I. Dzyaloshinsky, *A thermodynamic theory of weak ferromagnetism of antiferromagnetics*, J. Phys. Chem. Solids **4**, 241 (1958).

[31] T. Moriya, *Anisotropic superexchange interaction and weak ferromagnetism*, Phys. Rev. **120**, 91 (1960).

[32] T. Kurumaji, T. Nakajima, M. Hirschberger, A. Kikkawa, Y. Yamasaki, H. Sagayama, H. Nakao, Y. Taguchi, T.-h. Arima, and Y. Tokura, *Skyrmion lattice with a giant topological Hall effect in a frustrated triangular-lattice magnet*, Science **365**, 914 (2019).

[33] M. Hirschberger, L. Spitz, T. Nomoto, T. Kurumaji, S. Gao, J. Masell, T. Nakajima, A. Kikkawa, Y. Yamasaki, H. Sagayama, H. Nakao, Y. Taguchi, R. Arita, T.-h. Arima, and Y. Tokura, *Topological Nernst Effect of the Two-Dimensional Skyrmion Lattice*, Phys. Rev. Lett. **125**, 076602 (2020).

[34] T. Nomoto, T. Koretsune, and R. Arita, *Formation Mechanism of the Helical Q Structure in Gd-Based Skyrmion Materials*, Phys. Rev. Lett. **125**, 117204 (2020).

[35] M. Hirschberger, T. Nakajima, S. Gao, L. Peng, A. Kikkawa, T. Kurumaji, M. Kriener, Y. Yamasaki, H. Sagayama, H. Nakao, K. Ohishi, K. Kakurai, Y. Taguchi, X. Yu, T.-h. Arima, and Y. Tokura, *Skyrmion phase and competing magnetic orders on a breathing kagome lattice*, Nat. Commun. **10**, 5831 (2019).

[36] N. D. Khanh, T. Nakajima, X. Yu, S. Gao, K. Shibata, M. Hirschberger, Y. Yamasaki, H. Sagayama, H. Nakao, L. Peng, K. Nakajima, R. Takagi, T.-h. Arima, Y. Tokura, and S. Seki, *Nanometric square skyrmion lattice in a centrosymmetric tetragonal magnet*, Nat. Nanotech. **15**, 444 (2020).

[37] Y. Yasui, C. J. Butler, N. D. Khanh, S. Hayami, T. Nomoto, T. Hanaguri, Y. Motome, R. Arita, T. h. Arima, Y. Tokura, and S. Seki, *Imaging the coupling between itinerant electrons and localised moments in the centrosymmetric skyrmion magnet $GdRu_2Si_2$*, Nat. Commun. **11**, 5925 (2020).

[38] T. Okubo, S. Chung, and H. Kawamura, *Multiple-q States and the Skyrmion Lattice of the Triangular-Lattice Heisenberg Antiferromagnet under Magnetic Fields*, Phys. Rev. Lett. **108**, 017206 (2012).

[39] A. O. Leonov and M. Mostovoy, *Multiply periodic states and isolated skyrmions in an anisotropic frustrated magnet*, Nat. Commun. **6**, 8275 (2015).

[40] S.-Z. Lin and S. Hayami, *Ginzburg-Landau theory for skyrmions in inversion-symmetric magnets with competing interactions*, Phys. Rev. B **93**, 064430 (2016).

[41] S. Hayami, S.-Z. Lin, and C. D. Batista, *Bubble and skyrmion crystals in frustrated magnets with easy-axis anisotropy*, Phys. Rev. B **93**, 184413 (2016).

[42] C. D. Batista, S.-Z. Lin, S. Hayami, and Y. Kamiya, *Frustration and chiral orderings in correlated electron systems*, Rep. Prog.

Phys. **79**, 084504 (2016).

[43] I. Martin and C. D. Batista, *Itinerant Electron-Driven Chiral Magnetic Ordering and Spontaneous Quantum Hall Effect in Triangular Lattice Models*, Phys. Rev. Lett. **101**, 156402 (2008).

[44] Y. Akagi, M. Udagawa, and Y. Motome, *Hidden Multiple-Spin Interactions as an Origin of Spin Scalar Chiral Order in Frustrated Kondo Lattice Models*, Phys. Rev. Lett. **108**, 096401 (2012).

[45] S. Hayami and Y. Motome, *Multiple-Q instability by (d-2)-dimensional connections of Fermi surfaces*, Phys. Rev. B **90**, 060402 (2014).

[46] S. Hayami, R. Ozawa, and Y. Motome, *Effective bilinear-biquadratic model for noncoplanar ordering in itinerant magnets*, Phys. Rev. B **95**, 224424 (2017).

[47] R. Ozawa, S. Hayami, and Y. Motome, *Zero-Field Skyrmions with a High Topological Number in Itinerant Magnets*, Phys. Rev. Lett. **118**, 147205 (2017).

[48] S. Hayami and Y. Motome, *Néel- and Bloch-Type Magnetic Vortices in Rashba Metals*, Phys. Rev. Lett. **121**, 137202 (2018).

[49] S. Hayami, *Multiple-Q magnetism by anisotropic bilinear-biquadratic interactions in momentum space*, J. Mag. Mag. Mater. **513**, 167181 (2020).

[50] Y. Su, S. Hayami, and S.-Z. Lin, *Dimension transcendence and anomalous charge transport in magnets with moving multiple-Q spin textures*, Phys. Rev. Research **2**, 013160 (2020).

[51] S. Hayami, R. Ozawa, and Y. Motome, *Engineering chiral density waves and topological band structures by multiple-Q superpositions of collinear up-up-down-down orders*, Phys. Rev. B **94**, 024424 (2016).

[52] M. A. Ruderman and C. Kittel, *Indirect Exchange Coupling of Nuclear Magnetic Moments by Conduction Electrons*, Phys. Rev. **96**, 99 (1954).

[53] T. Kasuya, *A Theory of Metallic Ferro- and Antiferromagnetism on Zener's Model*, Prog. Theor. Phys. **16**, 45 (1956).

[54] K. Yosida, *Magnetic Properties of Cu-Mn Alloys*, Phys. Rev. **106**, 893 (1957).

[55] D. Khomskii and M. Mostovoy, *Orbital ordering and frustrations*, J. Phys. A **36**, 9197 (2003).

[56] Y.-D. Li, X. Wang, and G. Chen, *Anisotropic spin model of strong spin-orbit-coupled triangular antiferromagnets*, Phys. Rev. B **94**, 035107 (2016).

[57] S. Hayami and Y. Motome, *Effect of magnetic anisotropy on skyrmions with a high topological number in itinerant magnets*, Phys. Rev. B **99**, 094420 (2019).

[58] F. Eriksson, *On the measure of solid angles*, Math. Mag. **63**, 184 (1990).

[59] D. Solenov, D. Mozyrsky, and I. Martin, *Chirality Waves in Two-Dimensional Magnets*, Phys. Rev. Lett. **108**, 096403 (2012).

[60] R. Ozawa, S. Hayami, K. Barros, G.-W. Chern, Y. Motome, and C. D. Batista, *Vortex Crystals with Chiral Stripes in Itinerant Magnets*, J. Phys. Soc. Jpn. **85**, 103703 (2016).

[61] R. Yambe and S. Hayami, *Double-Q Chiral Stripe in the d–p Model with Strong Spin–Charge Coupling*, J. Phys. Soc. Jpn. **89**, 013702 (2020).

[62] S. Hayami and R. Yambe, *Degeneracy Lifting of Néel, Bloch, and Anti-Skyrmion Crystals in Centrosymmetric Tetragonal Systems*, J. Phys. Soc. Jpn. **89**, 103702 (2020).

[63] S.-Z. Lin, A. Saxena, and C. D. Batista, *Skyrmion fractionalization and merons in chiral magnets with easy-plane anisotropy*, Phys. Rev. B **91**, 224407 (2015).

[64] X. Z. Yu, W. Koshibae, Y. Tokunaga, K. Shibata, Y. Taguchi, N. Nagaosa, and Y. Tokura, *Transformation between meron and skyrmion topological spin textures in a chiral magnet*, Nature **564**, 95 (2018).

[65] B. Göbel, A. Mook, J. Henk, I. Mertig, and O. A. Tretiakov, *Magnetic bimerons as skyrmion analogues in in-plane magnets*, Phys. Rev. B **99**, 060407 (2019).

[66] S. Bera and S. S. Mandal, *Theory of the skyrmion, meron, antiskyrmion, and antimeron in chiral magnets*, Phys. Rev. Research **1**, 033109 (2019).

[67] S. Okumura, S. Hayami, Y. Kato, and Y. Motome, *Magnetic hedgehog lattices in noncentrosymmetric metals*, Phys. Rev. B **101**, 144416 (2020).

[68] D. Amoroso, P. Barone, and S. Picozzi, *Spontaneous skyrmionic lattice from anisotropic symmetric exchange in a Ni-halide monolayer*, arXiv:2005.02714 (2020).

[69] S. Hayami and Y. Motome, *Noncoplanar multiple-Q spin textures by itinerant frustration: Effects of single-ion anisotropy and bond-dependent anisotropy*, arXiv:2011.13040 (2020).

[70] Z. Wang, Y. Su, S.-Z. Lin, and C. D. Batista, *Skyrmion Crystal from RKKY Interaction Mediated by 2D Electron Gas*, Phys. Rev. Lett. **124**, 207201 (2020).